Half-Vortex Polariton Condensate in a Topological BIC Metasurface

Andrea Zacheo[1,2], Marco Marangi[1,2], Nilo Mata-Cervera[1,2], Yijie Shen[1,2], Giorgio Adamo[1,2], Cesare Soci[1,2,*]

[1] *Centre for Disruptive Photonic Technologies, The Photonics Institute, Nanyang Technological University, Singapore 637371*

[2] *Division of Physics and Applied Physics, School of Physical and Mathematical Sciences, Nanyang Technological University, Singapore 637371*

**Email : csoci@ntu.edu.sg*

Spin-orbit coupling in exciton-polariton condensates governs spinor interactions among quasi-particles and shapes the emergence of topological excitations, such as vortices, solitons, and strings. Conventional approaches to generate and manipulate these excitations rely on external gauge fields and structured light modulation, or microcavity TE-TM polarization splitting. While the former can only access the polariton pseudospin indirectly, through separate coupling of the excitonic or photonic component, the latter suffers from a lack of deterministic control over the resulting topological defects. Here, we report the generation of topology-induced spin polaritons in a monolithic bound state in the continuum (BIC) perovskite metasurface with broken inversion symmetry. Upon condensation, spin-momentum locking enables the generation of a pair of half-vortex within the polariton fluid, which display mutual attraction due to the connecting polarization string linking their opposite spins. We find that an increase in polariton density, enhancing the characteristic blueshift of the emission spectrum, leads to a narrowing of the inter-vortex separation, revealing deterministic interactions pinned to the cavity topology. By harnessing structural control alone, our approach enables robust engineering of the intrinsic pseudospin texture of the polariton fluid, offering a versatile platform for manipulating vortex nucleation, interaction, and annihilation without employing external fields.

Keywords: *monolithic perovskite metasurface, topology engineering, spin-orbit interactions, bound state in the continuum, spin texture, exciton-polariton condensate, quantum fluid, half-vortices*

Introduction

Vortices and topological charges have often been used as a unifying concept across physics, spanning from subatomic particles[1] and quantum fluids[2–5] to non-linear optics[6,7] and cosmology[8,9]. Vortices are defined as 2π-multiple integers winding of the phase of the wavefunction across a point-like singularity[10]. The energy flow rotates around the vortex core, that is the region where the rotational velocity formally diverges to infinite and the density of particles reaches the minimum, while the circulation direction determines the sign of the associated topological charge[11]. In polariton systems, vortices have been extensively investigated in excitonic quantum wells embedded in microcavities, where, by analogy with quantum fluidity (i.e. a superfluid), they are treated as point-like, quantized quasiparticles. Fundamental studies have focused on vortices within the "hydrodynamic" approximation such as full vortices[12,13], half vortices[14], spin vortices[15,16], and on fluctuation-generated vortices like the ones observed during Berezinsky-Kosterlitz-Thouless (BKT) transition[17]. In this context, the pseudospin, defined as a coordinate on the Poincaré sphere, provides an effective representation of the polariton's combined spin and polarization state, offering a natural framework to describe the formation and dynamics of related vortices[18]. The control of the spin degree of freedom and vortex generation in microcavity polariton condensates has been achieved by employing either inhomogeneous[19] or structured excitation sources, which entail topological singularities[20,21], by integrating spin-selective optical elements like nematic crystals[22–25], or by employing an external magnetic[26] or electric field[27]. These strategies are inherently limited to access only one components of the hybrid particles, either the photonic or the excitonic one. Consequently, they do not act on the polariton as a whole, preventing full manipulation of their hybrid pseudospin and reducing the possibilities to engineer more complex phenomena. In addition, TE-TM polarization splitting in microcavities which defines two nondegenerate polarization directions relative to the in-plane wavevector[28,29], offers only a weak and indirect control over the pseudospin[30,31], resulting in stochastic or non-deterministic vortex formation[32]. Recently, photonic metasurfaces supporting optical bound states in the continuum (BICs) have emerged as a versatile open cavity architecture to

enter the strong-coupling regime[33,34] and induce exciton-polariton condensation[35]. BICs are non-radiative states in the continuum spectrum protected by lattice symmetry, which manifest as dark modes at the Γ-point of the reciprocal space[36]. Due to the symmetry mismatch between the photonic mode profiles and the out-of-plane propagating waves, BICs are fully decoupled from the far field radiation and therefore cannot be accessed by external excitation[37]. This results in strong photon confinement in the near field and a theoretically infinite Q-factor of the cavity mode. Beyond this conventional symmetry-based picture, BICs can also be understood from a topological perspective: in momentum space, the far-field polarization winds around the BIC, forming a vortex whose charge is robust against continuous perturbations. As a result, optical BICs carry an invariant integer topological charge, defined by the winding number of the polarization director, analogous to quantized vortices in quantum fluids[38]. When the in-plane symmetry is broken, these ideal BICs acquire a finite radiative linewidth, and their resonance Q-factor is correspondingly reduced. The resulting modes, now weakly coupled to the far-field, are referred to as *quasi*-BICs (*q*BICs). Importantly, the nature of symmetry-breaking also determines the spin texture of the radiated field. With appropriately engineered perturbations, *q*BICs can exhibit spin-selective emission and momentum-dependent splitting of their dispersion, an optical analogue of the electronic Rashba effect[39]. These features become particularly compelling for BIC metasurfaces fabricated directly in strongly excitonic media where the spatial and energetic overlap between photons and excitons is maximized. In this case, the metasurface geometry not only governs the photonic mode structure but also provides selective control over the polariton pseudospin through precise design of the underlying symmetry. Among the available material platforms, halide perovskites (hybrid organic-inorganic semiconductors with strong exciton binding energy, high luminescence, and tunable bandgap) have emerged as ideal candidates for the realization of both optically[40] and electrically[41] driven monolithic BIC metasurfaces. In these systems, exciton-polariton formation[42], condensation[43] and emission carrying spin[44] and topological charges[45] have all been recently demonstrated. Here, we exploit a *q*BIC monolithic perovskite metasurface with out-of-plane broken symmetry to demonstrate direct

access to (and control of) the intrinsic polariton pseudospin, as evidenced by the appearance of a stable half vortex-antivortex (V-AV) pair in the condensate emission, each carrying opposite topological charge. Spin-momentum locking enables control of the total topological charge from the unitary charge of the V-AV pair to the vanishing charge resulting from their mutual annihilation. Power dependent measurements unveil the spatial evolution of the V-AV separation, governed by the spin texture of the condensate. This evolution is accompanied by the emergence of a connecting polarization string, arising from a π rotation of the pseudospin, which defines both the direction and the strength of the mutual interaction between the two half-vortices. By leveraging metasurface design to selectively control spin and orbital angular momentum of polariton condensates in both momentum and real space, our approach provides a versatile platform for exploring collective quantum phenomena in polariton fluids and for realizing optically and electrically driven topological devices and coherent light sources.

Symmetry breaking in *q*BIC metasurface induces spin-orbit coupling in exciton-polaritons

We engineered a dielectric metasurface, consisting of isosceles triangular holes arranged in a square lattice, carved directly in a polycrystalline methylammonium lead iodide ($MAPbI_3$) film (see Methods and *Supplementary Information, Section 1*) coated on a SiO_2/Si substrate (**Fig. 1a**). Due to their geometric rotational asymmetry, the isosceles triangles intrinsically disrupt the twofold rotational invariance of the structure[46], enabling the mode transition from a symmetry protected BIC with the characteristic vortex-like (V-point) polarization singularity, to a symmetry-broken *q*BIC, with two distinct and opposite spin states, $\sigma^+$and σ^-, located off the centre (Γ–point) of the momentum space (*Supplementary Information, Section 2*). Thanks to the high-Q factor and the good spatial overlap, the *q*BIC mode strongly couples with the $MAPbI_3$ film, forming exciton polaritons that undergo condensate phase transition at high excitation fluence. The two opposite spin-polarized polariton states carry a half-integer topological charge $p = \pm\frac{1}{2}$ associated with a π rotation of the polarization

ellipse, and an integer topological charge $q = \pm 1$ related to the winding of their phase. This results in circularly polarized condensate emission with opposite handedness and high spin purity, in counter-propagating, momentum-locked directions (**Fig. 1b**).

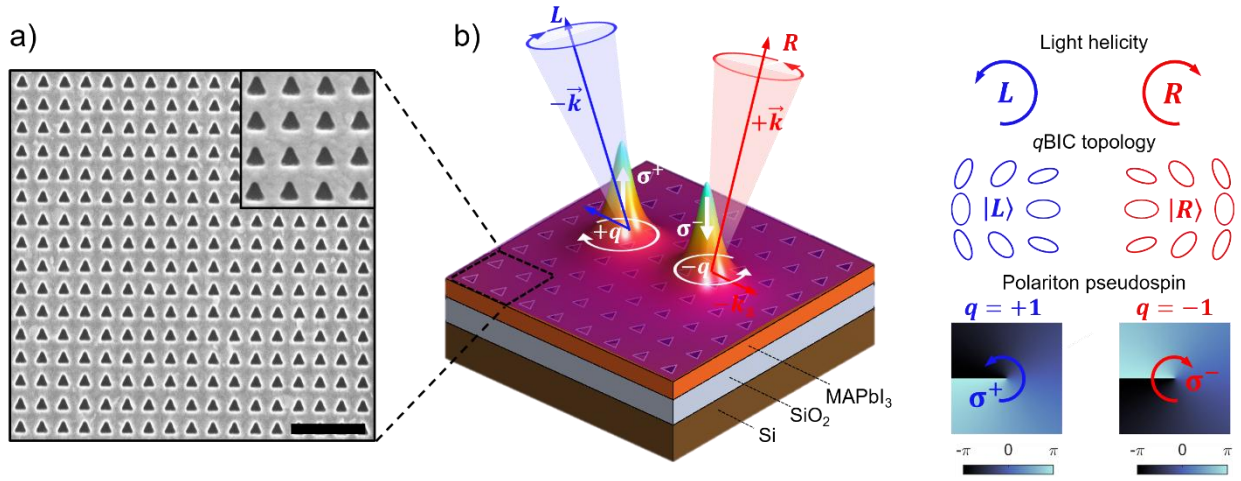

Figure 1. Spin-orbit coupling of exciton-polaritons from broken inversion symmetry BIC metasurface: (a) Scanning electron microscope (SEM) image of the monolithic perovskite square lattice metasurface with isosceles triangular holes (scale bar 1 μm). The inset shows a magnified view of the triangular metamolecules. **(b)** Breaking of the in-plane C_2 symmetry splits the BIC resonance into a pair of opposite circularly polarized states $\sigma^+$and σ^-, enabling the formation of a spin-orbit coupled exciton-polariton condensate with half-integer topological charges $p = \pm\frac{1}{2}$ in the polarization domain, and integer charges $q = \pm 1$ in the phase domain.

Spin-polarized *q*BIC exciton-polariton condensate

The interaction between the $MAPbI_3$ exciton and the uncoupled *q*BIC can be tailored by tuning the metasurface geometrical parameters to maximize their mutual overlap and enable formation of hybrid polariton states with high spin purity. **Figure 2** shows the emergence of strong-coupling and the transition of the exciton-polariton to a condensate state through simulated and experimental angle-resolved spectra of the metasurface. The energy-momentum maps of numerically calculated transverse-electric (TE) transmittance (**Fig. 2a**) and the experimental photoluminescence (**Fig. 2b**), measured using a Fourier imaging setup (*Supplementary Information, Section 4*), show the

appearance of a clear *q*BIC band below the $MAPbI_3$ exciton (1.685 eV at 77 K, green dotted line in **Fig. 2b**). Fitting of the measured bands with a coupled oscillator model between the $MAPbI_3$ exciton and the uncoupled *q*BIC resonance (white dotted line in **Fig. 2b**) captures well the experimental band dispersion and predicts the formation of upper (UP) and lower (LP) exciton-polariton bands (white dashed lines in **Fig. 2b**) with a Rabi splitting of $\hbar\Omega = 102$ meV. Only the lower polariton branch is visible due to the strong absorption of the perovskite at energies above the exciton line. A detailed description of the fitting procedure is provided in *Section 3* of the *Supplementary Information*. By increasing the excitation fluence, polaritons undergo a condensation phase transition, evidenced by the localization of light emission near the Γ-point (**Fig. 2c**). This coincides with the onset of polariton lasing at a threshold $P_{th} \cong 26.9\ \mu J/cm^2$, with characteristic sigmoidal shape of the light-light curve, narrowing of the FWHM and spectral blueshift. The polariton laser shows extended spatial and temporal coherence around $10\ \mu m$ and 500 fs , respectively (*Supplementary Information, Section 4*). The monolithic integration of the metasurface within the perovskite film results in a reduced condensation threshold and increased spatial coherence length compared to what observed in similar polycrystalline films coupled to dielectric metasurfaces[47], owing to the reduced spatial inhomogeneities enabled by the monolithic design. As expected from the in-plane inversion symmetry breaking in the *q*BIC metasurfaces, the polariton bands show a high degree of polarization, with strong dichroism appearing between modes emitted in opposite directions relative to the centre of the Brillouin zone. To map the location of the two points with circular polarization in the momentum space (C-points in the Poincaré sphere), we retrieved the Stokes parameters along the lower polariton branch from eigenfrequency simulations. Starting from large k values, the ellipticity first changes sign and then reduces approaching the Γ-point , becoming circular ($|S_3| = 1$) at $k_x = \pm 0.38\ \mu m^{-1}$ (**Fig. 2d**). The experimental S_3 parameters agree well with the trend predicted by numerical simulations, yielding polariton pseudospin purity of $|S_3| \sim 0.6$ below threshold (**Fig. 2e**). Above the excitation threshold, polariton condensation occurs exactly at the momentum-space locations corresponding to the C-points, and the spin purity increases to $|S_3| \sim 0.85$ (**Fig. 2f**). This

indicates successful excitation of polariton condensates with well-defined pseudospin directly connected to the topology of the metasurface. The slight residual ellipticity can be attributed to fabrication imperfections.

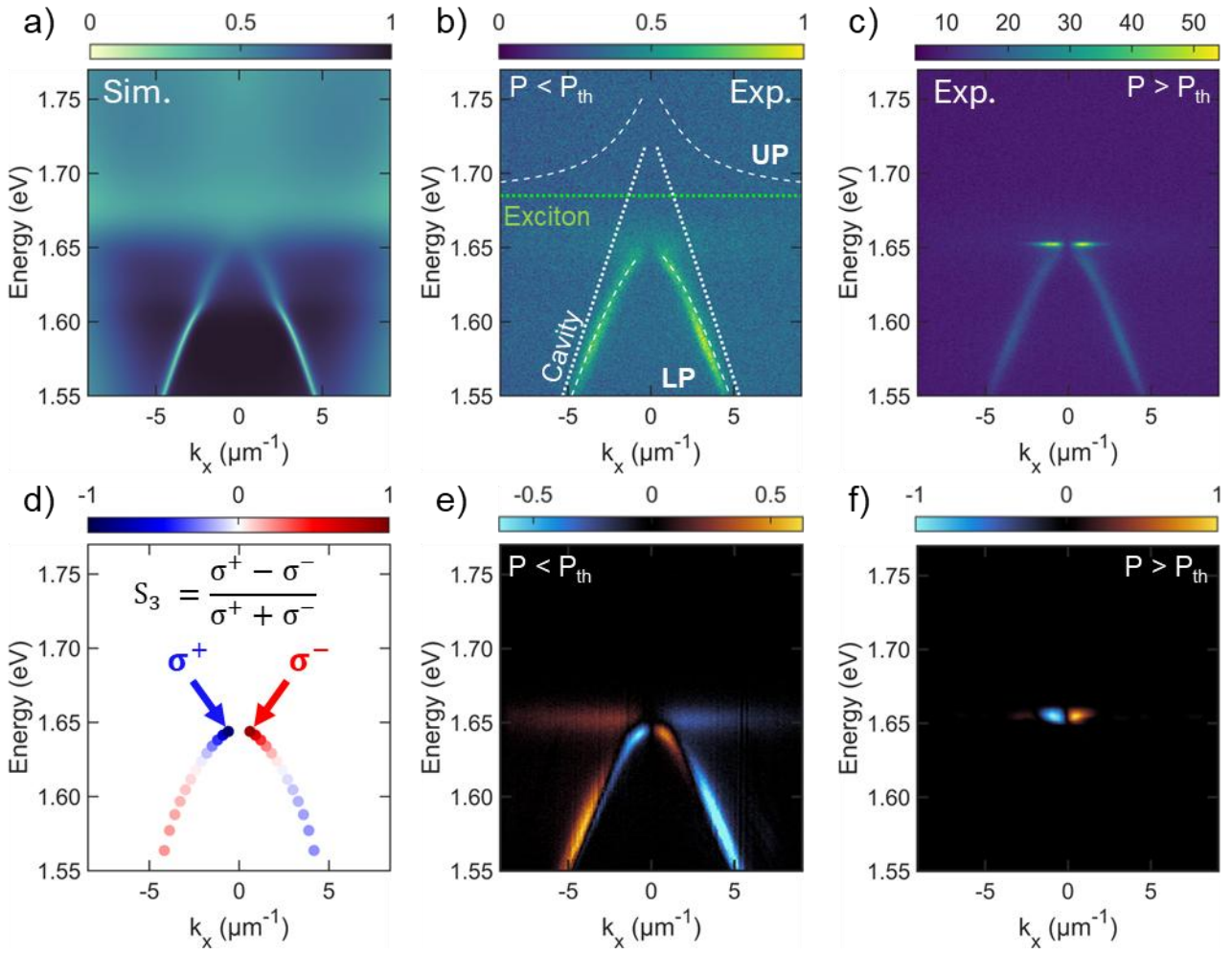

Figure 2. Characterization of spin-polarized *q*BIC-polariton condensate: (a) Simulated transmittance and **(b)** measured photoluminescence angle-resolved spectra of the *q*BIC metasurface showing anticrossing and the formation of the lower exciton-polariton branch. The uncoupled cavity resonance (white dotted line) and the $MAPbI_3$ exciton (1.685 eV, green dotted line) in **(b)** are used to fit the polariton bands (white dashed lines) through a coupled oscillator model. **(c)** Above the excitation threshold $P_{th} = 26.9\ uJ/cm^2$, the system exhibits condensate phase transition with the characteristic BIC emission lobes localized near the center of the reciprocal space. **(d)** Numerical simulations predict spin anisotropy of the band in the momentum space, that it is successfully imprinted to the LP emission below threshold **(e)** and to its condensate phase **(f)**.

Half-vortices in the *q*BIC condensate emission

Half-vortices in polariton condensates were initially predicted by *Y. Rubo* for an equilibrium spinorial fluid[48], and subsequently observed experimentally in CdTe/CdMgTe microcavities under non-resonant excitation[49]. A half-vortex is characterized by a phase singularity in only one circular polarization and is described by two winding numbers (k, m), where k and m denote the winding of the polarization angle and the phase, respectively, both changing simultaneously by $\pm\pi$[50]. In our system, the *q*BIC metasurface directly imprints a spin-momentum locked polarization texture onto the polariton field with a π variation between the C-points (**Fig. S2d**), matching the conditions for such topological defects to emerge. This directly leads to the formation of spatially separated, oppositely charged half-vortices, as confirmed by numerical simulations and Stokes polarimetry of the condensate emission (*Supplementary Information, Sections 6 and 7*), with their positions in momentum space pinned by the underlying pseudospin texture. The spatial phase of the condensate is investigated via Michelson interferometry **(Fig. S4**), enabling reconstruction of the wavefront in a selectively chosen polarization basis. In real space, the condensate emission forms two lobes with opposite circular polarization, separated by a dark region characterized by linear polarization, corresponding to the long lifetime *q*BIC dark state (**Figure 3**). Vortex topological charge summation can be achieved by interfering the portion of the emission with the same spin state, σ^+ (**Fig. 3a)** or σ^- (**Fig. 3d)**. This is obtained by selecting the spin state through appropriately aligned quarter waveplate and polarizer, splitting the signal in two arms, and allowing the interference between points $\mathbf{r_1} = (\mathrm{r_x}, \mathrm{r_y})$ of the original signal L1 (R1), and points $\mathbf{r_2} = (\mathrm{r_x}, -\mathrm{r_y})$ of the retroreflected wavefront L2 (R2). The interference fringes are generated by the phase difference between the two beams and the presence of bifurcations, seen in **Figs. 3b, e**, indicate the existence of vortex phase singularities. The maps of the phase difference between signals on the two arms, $\Delta\phi = \varphi_1 - \varphi_2$, confirm the presence of spatially-separated phase vortices carrying opposite topological charges, with the σ^+ component exhibiting a positive charge, $q = +1$ (**Fig. 3c**), and the σ^- component a negative

charge, $q = -1$ (**Fig. 3f**). The two vortices seen in each phase maps belong to the signal (L1 or R1) and retroreflected (L2 or R2) beam and carry the same charge because of the mirror flipping introduced by the interferometer arms. Interestingly, V-AV annihilation can be achieved if the beams are interfered preserving the opposite sign of their topological charges. This is achieved by simply mirroring the retroreflected image as $\mathbf{r_2} = (-r_x, r_y)$, as illustrated in **Fig. 3g**. This configuration gives rise to vertical interference fringes (**Fig. 3h**) with no dislocations, confirming annihilation of the vortices (**Fig. 3i**). These experiments unambiguously confirm that the condensate half V-AV pair is generated by the inherent spin-orbit interaction in the metasurface and indicate that cavity-engineering is a viable route to control topological charges in polariton condensates.

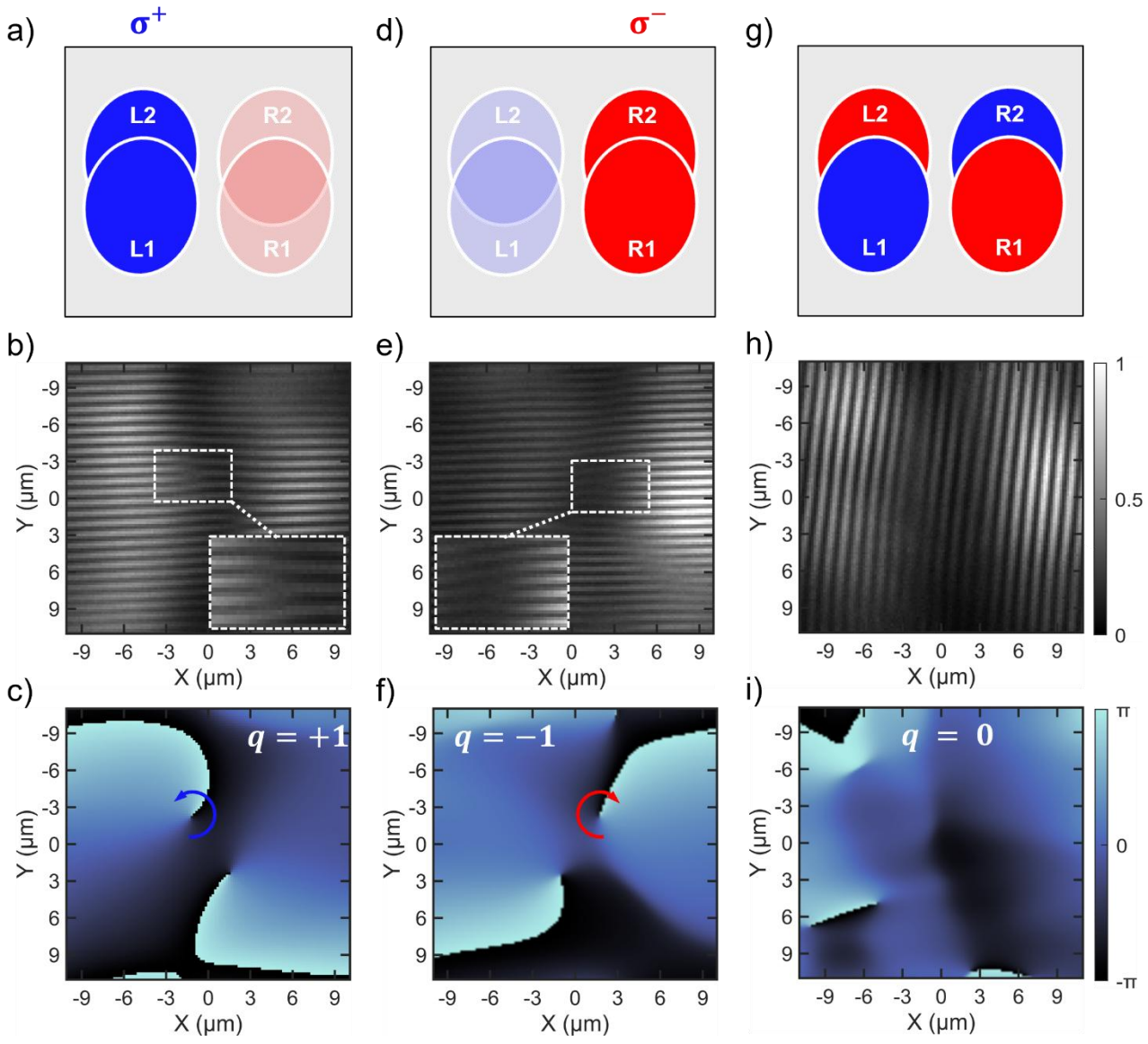

Figure 3. Real space half-vortices observation in qBIC polariton condensate: (a) Schematic of the Michelson interferometer configuration, where the lobe with left circular polarization L1 is interfered with its retroreflected image L2. **(b)** The horizontal interference fringes present characteristic bifurcations patterns (inset shows magnified view of the bifurcation region) and **(c)** the retrieved phase map reveals the presence of vortices carrying a topological charge $q = +1$. **(d)** Same interferometer configuration of **(a)** for the lobe with the right circular polarization R1 interfered with R2, showing opposite bifurcation patterns in the interference fringes **(e)** and vortices with topological charge $q = -1$ **(f)**. **(g)** Spatial overlap of emission lobes with opposite polarization, achieved rotating the retroreflector by 90°, results in **(h)** vertical interference fringes without any bifurcations and **(i)** complete vortex annihilation with net topological charge of $q = 0$.

Interacting vortices in a *q*BIC metasurface

Spin plays a major role in determining the interactions between polaritons in a condensate. In general, polaritons with spin of the same sign repel each other, while those with opposite sign attract[51]. These attractive and repulsive interactions are directly reflected into vortices dynamics, that undergo repulsion and attraction according to the sign of the topological charges they carry[52]. Theoretical models, based on the spin-dependent Gross–Pitaevskii equation, predict that attractive and repulsive interactions have comparable strength[53]. Meanwhile, temporal dynamics reveal that vortices are not spatially pinned in time, but their positions and angular orientations follow complex trajectories that depends on the nature of the vortices, the initial injection conditions, and the condensate particle density[54]. For polariton spin texture that enables the formation of topological half vortices, the region where the polarization angle travels an arc of length $\pm\pi$, defines a string (or soliton) attached to the half vortices[55]. The string can connect half-vortices with opposite sign, leading to mutual interactions with strength proportional to the length of the string. In light of these observations, we conducted a power-dependent study to characterize the evolution of the V-AV pair interaction in our *q*BIC metasurface. To visualize both vortices simultaneously, we interfere the beam with its mirror image, i.e. we combined the cases analysed in **Fig. 3a, b**. The measurements reveal that the mutual distance

d between vortex and antivortex, extracted from the phase maps (**Fig. 4a-c**), decreases with increasing excitation fluence (**Fig. 4a-d**), and is accompanied by a corresponding increase in the interaction strength (expressed through the blueshift observed in **Fig. 4e**), indicating an overall attractive trend within the V-AV pair. Assuming the characterization of vortices in conventional microcavity polariton condensates also applies to our qBIC system, the healing length, defined as the length scale where the kinetic energy is balanced by the interaction energy, can be written as $\xi(\mu\text{m}) = \hbar/\sqrt{2m_{LP}^{*}\Delta\text{E}}$, where m_{LP}^{*} is the effective mass of the lower polariton branch and ΔE the spectral blueshift. This quantity is comparable to the vortex core radius $r \cong 1.7$ μm (see real space images in *Supplementary Information, Section 8*), indicating that vortices preserve their phase over the maximum displacement $\Delta\text{d}\sim 2$ μm observed within the range of excitation fluences investigated (**Fig. 4f**). While the vortex pair originates from the qBIC topology, the increase in condensate population density and the occupation of multiple states with opposite spin can lead to a diffusion-like displacement of their cores in real space. This behaviour is consistent with the half-vortex model with an attached string described in Ref. 55 and is also supported by the close correspondence between the measured vortex displacement and the calculated healing length, within the microcavity approximation. However, the observed dynamics of the spin vortices cannot be attributed solely to attractive forces: their complex orbital motion can produce transient approaches that, at different pump powers, manifest as an apparent gradual attraction. Additionally, the presence of structural disorder or local defects can perturb the vortex positions, contributing to variations in their observed separation and dynamics. Time-resolved measurements would be required to disentangle the contribution of purely attractive interactions from that of other orbital effects and would constitute a compelling subject for further studies.

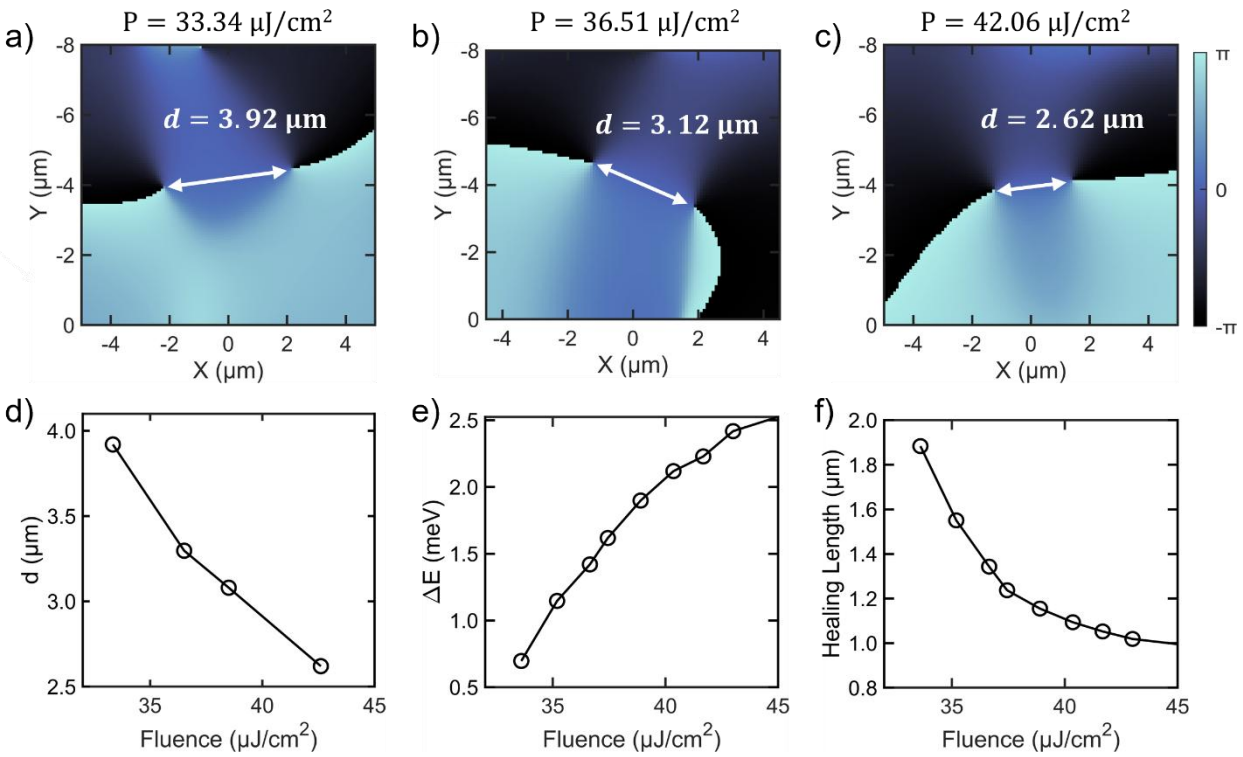

Figure 4. Vortices inter-distance evolution at different fluences: (a-c) Phase maps of condensate emission at different pump fluences. **(d)** Measured distances between opposite charged vortices as function of the fluence, showing an approaching trend. **(e)** Extracted blueshift and **(f)** calculated healing length of the qBIC polariton condensate.

Conclusion

We have demonstrated the generation of a half-vortex polariton condensate pinned to the topology of a *q*BIC monolithic perovskite metasurface with broken in-plane inversion symmetry. The spin selectivity, enabled by the *q*BIC, and transferred to the exciton-polaritons via strong coupling, provides control over the condensate's spin textures and vortex dynamics, as evidenced by vortex-antivortex annihilation and power-dependent vortex attraction. This constitutes a significant paradigm shift from conventional methods, which require external artificial fields, such as structured light, magnetic fields, or liquid crystals, and shows that the manipulation of topological excitations in polariton condensates can be achieved solely through cavity engineering. Our results establish *q*BIC metasurfaces as a versatile platform for exploring advanced polaritonic phenomena, including spin

Hall[56] and meron Hall[57] currents, stable vortex crystals[58], and vortex molecules[59], potentially enabling their application in information encoding schemes[60], and the realization of all-optical logic operations[61,62].

Methods

Metasurface design

The quasi-bound state in the continuum supporting metasurface was designed via Finite Difference Time Domain (FDTD) and Rigorous Coupled-Wave Analysis (RCWA) suit of the commercial software Ansys Lumerical. The adopted triangular geometry supports an out-of-plane magnetic H_z quadrupole resonance with an asymmetric distribution in the x-y plane dictated by the broken in-plane inversion symmetry of the design (*Supplementary Information*, *Section 2*). COMSOL Multiphysics eigenfrequency solver has also utilized to calculate the quality factor and the complex electric field of the resonance at multiple angles.

Polycrystalline $MAPbI_3$ film deposition and metasurface fabrication

$MAPbI_3$ films were fabricated from a 0.5 M precursor solution of CH_3NH_3I (Dyesol, Greatcell) and PbI_2 (99.99%, Sigma-Aldrich) with a molar ratio 1:1, in anhydrous dimethylformamide (DMF, Sigma-Aldrich). The solution was magnetically stirred over night at 373 K in N_2 inert atmosphere glovebox and then filtered by a polyvinylidene fluoride (PVDF) syringe filter (0.45 μm) before spin-coating. Prior to deposition, the substrates were cleaned with ultrasonication for 5 min in acetone and isopropanol, respectively. Subsequently, substrates were dried with nitrogen, followed by 20 minutes ozone surface treatment. The perovskite precursor solution was spin-coated onto the Si/SiO_2 substrates with a speed of 4000 rpm for 35 s using the toluene anti-solvent deposition method, with the anti-solvent being drop-cast on the substrates 6 s after spinning began. The film was then annealed at 373K for 10 minutes, yielding a 131 nm thickness, as measured by atomic force microscopy (*Supplementary Information*, *Section 1*). The perovskite metasurface fabrication was conducted by

focused ion beam (FIB) lithography process. A 50 x 50 μm^2 triangular air holes array was patterned using the Helios 600 NanoLab, FEI system. The ion beam current was controlled around ~1.7 pA for suitable spot size of etching.

Angle-resolved spectroscopy

Angle-resolved reflectance (ARR) and photoluminescence (ARPL) measurements were performed with a custom-built micro-spectrometer setup consisting of an inverted optical microscope (Nikon Ti-u, 50x objective, NA=0.556), a spectrograph (Andor SR-303i with a 300 lines/mm grating), and a charged-coupled detector (CCD, Andor iDus 420). A series of lenses along the beam path between the microscope and the spectrograph projects the back focal plane (BFP) of the collection objective on the slit of the spectrograph, allowing the collection of angular information within bounds defined by k_x/k_0=NA=0.556. The sample was excited by a 400 nm femtosecond pulsed laser (Coherent) with 1 KHz repetition rate and beam diameter of 17 μm.

Measurements of spatial and temporal coherence

Spatial and temporal coherence of the condensate are inferred by the interference pattern formed in a standard Michelson interferometer (see *Supplementary Information*, *Section 4*), where the sample emission is split into two arms by a 50/50 beamsplitter. The two arms are mounted on translating stages to spatially and temporally overlap the reflect images with a retroreflector and a mirror to form interference fringes. The retroreflector is mounted on a coarse alignment stage, while the mirror is mounted on a precision micrometre actuator with 1 μm resolution (model SM1ZA). The two arms are then recombined on a CMOS camera (model CS165MU).

Author contributions

A.Z. G.A. and C.S. conceived the idea. A.Z. carried out design optimisation and fabrication of the perovskite metasurfaces and conducted spectroscopy measurements and data analysis with the help of M.M and G.A.. A.Z. and N.M.C. performed all numerical simulations. A.Z. drafted the manuscript and all authors contributed to editing and review. C.S. and G.A. supervised the work.

Acknowledgements

We are indebted to D. Sanvitto, D. Gerace, T.C.H. Liew and Y. Rubo for the insightful discussions and suggestions they provided with regard this work. Research was supported by the Singapore Ministry of Education (Grant no. MOE-T2EP50222-0015) and the National Research Foundation through the National Centre for Advanced Integrated Photonics (Grant no. NRF-MSG-2023-0002).

References

1. Luski, A. *et al.* Vortex beams of atoms and molecules. *Science* **373**, 1105–1109 (2021).
2. Bardeen, J. & Stephen, M. J. Theory of the Motion of Vortices in Superconductors. *Phys. Rev.* **140**, A1197–A1207 (1965).
3. Pitaevskiĭ, L. P. & Stringari, S. *Bose-Einstein Condensation*. (Clarendon Press, Oxford ; New York, 2003).
4. Abrikosov, A. A. Nobel Lecture: Type-II superconductors and the vortex lattice. *Rev. Mod. Phys.* **76**, 975–979 (2004).
5. Carusotto, I. & Ciuti, C. Quantum fluids of light. *Rev. Mod. Phys.* **85**, 299–366 (2013).
6. Willner, A. E., Wang, J. & Huang, H. A Different Angle on Light Communications. *Science* **337**, 655–656 (2012).
7. Molina-Terriza, G., Torres, J. P. & Torner, L. Twisted photons. *Nat. Phys.* **3**, 305–310 (2007).
8. Abbott, B. P. *et al.* Observation of Gravitational Waves from a Binary Black Hole Merger. *Phys. Rev. Lett.* **116**, 061102 (2016).
9. Liberati, S. & Maccione, L. Astrophysical Constraints on Planck Scale Dissipative Phenomena. *Phys. Rev. Lett.* **112**, 151301 (2014).
10. Kivshar, Y. S. Optical vortices and vortex solitons. in (eds McCall, M. W. & Dewar, G.) 16 (Denver, CO, 2004). doi:10.1117/12.560688.
11. Matthews, M. R. *et al.* Vortices in a Bose-Einstein Condensate. *Phys. Rev. Lett.* **83**, 2498–2501 (1999).
12. Lagoudakis, K. G. *et al.* Quantized vortices in an exciton–polariton condensate. *Nat. Phys.* **4**, 706–710 (2008).
13. Cancellieri, E. *et al.* Merging of vortices and antivortices in polariton superfluids. *Phys. Rev. B* **90**, 214518 (2014).
14. Dominici, L. *et al.* Vortex and half-vortex dynamics in a nonlinear spinor quantum fluid. *Sci. Adv.* **1**, e1500807 (2015).
15. Manni, F., Léger, Y., Rubo, Y. G., André, R. & Deveaud, B. Hyperbolic spin vortices and textures in exciton–polariton condensates. *Nat. Commun.* **4**, 2590 (2013).
16. Borgh, M. O., Keeling, J. & Berloff, N. G. Spatial pattern formation and polarization dynamics of a nonequilibrium spinor polariton condensate. *Phys. Rev. B* **81**, 235302 (2010).
17. Caputo, D. *et al.* Topological order and thermal equilibrium in polariton condensates. *Nat. Mater.* **17**, 145–151 (2018).
18. Pavlovic, G., Malpuech, G. & Shelykh, I. A. Pseudospin dynamics in multimode polaritonic Josephson junctions. *Phys. Rev. B* **87**, 125307 (2013).

19. Roumpos, G. *et al.* Single vortex–antivortex pair in an exciton-polariton condensate. *Nat. Phys.* **7**, 129–133 (2011).

20. Pickup, L., Töpfer, J. D., Sigurdsson, H. & Lagoudakis, P. G. Polariton spin jets through optical control. *Phys. Rev. B* **103**, 155302 (2021).

21. Gnusov, I. *et al.* Quantum vortex formation in the “rotating bucket” experiment with polariton condensates. *Sci. Adv.* **9**, eadd1299 (2023).

22. Li, Y. *et al.* Manipulating polariton condensates by Rashba-Dresselhaus coupling at room temperature. *Nat. Commun.* **13**, 3785 (2022).

23. Łempicka-Mirek, K. *et al.* Electrically tunable Berry curvature and strong light-matter coupling in liquid crystal microcavities with 2D perovskite. *Sci. Adv.* **8**, eabq7533 (2022).

24. Liang, J. *et al.* Polariton spin Hall effect in a Rashba–Dresselhaus regime at room temperature. *Nat. Photonics* **18**, 357–362 (2024).

25. Zhai, X. *et al.* Electrically controlling vortices in a neutral exciton polariton condensate at room temperature. *Phys. Rev. Lett.* **131**, 136901 (2023).

26. Caputo, D. *et al.* Magnetic control of polariton spin transport. *Commun. Phys.* **2**, 165 (2019).

27. LaMountain, T. *et al.* Valley-selective optical Stark effect of exciton-polaritons in a monolayer semiconductor. *Nat. Commun.* **12**, 4530 (2021).

28. Panzarini, G. *et al.* Exciton-light coupling in single and coupled semiconductor microcavities: Polariton dispersion and polarization splitting. *Phys. Rev. B* **59**, 5082–5089 (1999).

29. Dufferwiel, S. *et al.* Spin Textures of Exciton-Polaritons in a Tunable Microcavity with Large TE-TM Splitting. *Phys. Rev. Lett.* **115**, 246401 (2015).

30. Shelykh, I. A., Kavokin, A. V., Rubo, Y. G., Liew, T. C. H. & Malpuech, G. Polariton polarization-sensitive phenomena in planar semiconductor microcavities. *Semicond. Sci. Technol.* **25**, 013001 (2010).

31. Spencer, M. S. *et al.* Spin-orbit–coupled exciton-polariton condensates in lead halide perovskites. *Sci. Adv.* **7**, eabj7667 (2021).

32. Manni, F. *et al.* Dissociation dynamics of singly charged vortices into half-quantum vortex pairs. *Nat. Commun.* **3**, 1309 (2012).

33. Dang, N. H. M. *et al.* Long-Range Ballistic Propagation of 80% Excitonic Fraction Polaritons in a Perovskite Metasurface at Room Temperature. *Nano Lett.* **24**, 11839–11846 (2024).

34. Sortino, L. *et al.* Atomic-layer assembly of ultrathin optical cavities in van der Waals heterostructure metasurfaces. *Nat. Photonics* **19**, 825–832 (2025).

35. Ardizzone, V. *et al.* Polariton Bose-Einstein condensate from a Bound State in the Continuum. *Nature* **605**, 447–452 (2022).

36. Hsu, C. W., Zhen, B., Stone, A. D., Joannopoulos, J. D. & Soljačić, M. Bound states in the continuum. *Nat. Rev. Mater.* **1**, 16048 (2016).

37. Koshelev, K. L., Sadrieva, Z. F., Shcherbakov, A. A., Kivshar, Yu. S. & Bogdanov, A. A. Bound states in the continuum in photonic structures. *Phys.-Uspekhi* **66**, 494–517 (2023).

38. Zhen, B., Hsu, C. W., Lu, L., Stone, A. D. & Soljačić, M. Topological Nature of Optical Bound States in the Continuum. *Phys. Rev. Lett.* **113**, 257401 (2014).

39. Tian, J. *et al.* Optical Rashba Effect in a Light-Emitting Perovskite Metasurface. *Adv. Mater.* **34**, 2109157 (2022).

40. Huang, C. *et al.* Ultrafast control of vortex microlasers. *Science* **367**, 1018–1021 (2020).

41. Wang, Y. *et al.* Directional Emission from Electrically Injected Exciton–Polaritons in Perovskite Metasurfaces. *Nano Lett.* **23**, 4431–4438 (2023).

42. Dang, N. H. M. *et al.* Realization of Polaritonic Topological Charge at Room Temperature Using Polariton Bound States in the Continuum from Perovskite Metasurface. *Adv. Opt. Mater.* **10**, 2102386 (2022).

43. Wu, X. *et al.* Exciton polariton condensation from bound states in the continuum at room temperature. *Nat. Commun.* **15**, 3345 (2024).

44. Wang, Y., Adamo, G., Ha, S. T., Tian, J. & Soci, C. Electrically Generated Exciton Polaritons with Spin On-Demand. *Adv. Mater.* **37**, 2412952 (2025).

45. Tian, J. *et al.* Phase-Change Perovskite Microlaser with Tunable Polarization Vortex. *Adv. Mater.* **35**, 2207430 (2023).

46. Liu, W. *et al.* Circularly Polarized States Spawning from Bound States in the Continuum. *Phys. Rev. Lett.* **123**, 116104 (2019).

47. Marangi, M., Zacheo, A., Dubrovkin, A. M., Adamo, G. & Soci, C. Exciton–polariton condensation in $MAPbI_3$ films from bound states in the continuum metasurfaces. *Nanophotonics* https://doi.org/10.1515/nanoph-2025-0128 (2025) doi:10.1515/nanoph-2025-0128.

48. Rubo, Y. G. Half Vortices in Exciton Polariton Condensates. *Phys. Rev. Lett.* **99**, 106401 (2007).

49. Lagoudakis, K. G. *et al.* Observation of Half-Quantum Vortices in an Exciton-Polariton Condensate. *Science* **326**, 974–976 (2009).

50. Toledo-Solano, M., Mora-Ramos, M. E., Figueroa, A. & Rubo, Y. G. Warping and interactions of vortices in exciton-polariton condensates. *Phys. Rev. B* **89**, 035308 (2014).

51. Gippius, N. A. *et al.* Polarization Multistability of Cavity Polaritons. *Phys. Rev. Lett.* **98**, 236401 (2007).

52. *Exciton Polaritons in Microcavities New Frontiers*. (Springer Berlin, Berlin, 2014).

53. Vladimirova, M. *et al.* Polariton-polariton interaction constants in microcavities. *Phys. Rev. B* **82**, 075301 (2010).

54. Dominici, L. *et al.* Interactions and scattering of quantum vortices in a polariton fluid. *Nat. Commun.* **9**, 1467 (2018).

55. Solano, M. T. & Rubo, Y. G. Vortices in exciton-polariton condensates with polarization splitting. *J. Phys. Conf. Ser.* **210**, 012024 (2010).

56. Kavokin, A., Malpuech, G. & Glazov, M. Optical Spin Hall Effect. *Phys. Rev. Lett.* **95**, 136601 (2005).

57. Rao, L. *et al.* Meron Spin Textures in Momentum Space Spawning from Bound States in the Continuum. *Phys. Rev. Lett.* **135**, 026203 (2025).

58. Liew, T. C. H., Rubo, Y. G. & Kavokin, A. V. Generation and Dynamics of Vortex Lattices in Coherent Exciton-Polariton Fields. *Phys. Rev. Lett.* **101**, 187401 (2008).

59. Hu, J. *et al.* Vortex molecules in exciton-polariton condensates formed by uniform nonresonant pumping. *Phys. Rev. B* **111**, 245119 (2025).

60. Kavokin, A. *et al.* Polariton condensates for classical and quantum computing. *Nat. Rev. Phys.* **4**, 435–451 (2022).

61. Ma, X. *et al.* Realization of all-optical vortex switching in exciton-polariton condensates. *Nat. Commun.* **11**, 897 (2020).

62. Ballarini, D. *et al.* All-optical polariton transistor. *Nat. Commun.* **4**, 1778 (2013).

Supplementary Information for:

Half-Vortex Polariton Condensate in a Topological BIC Metasurface

Andrea Zacheo[1,2], Marco Marangi[1,2], Nilo Mata-Cervera[1,2], Yijie Shen[1,2], Giorgio Adamo[1,2], Cesare Soci[1,2,*]

[1] *Centre for Disruptive Photonic Technologies, The Photonics Institute, Nanyang Technological University, Singapore 637371*

[2] *Division of Physics and Applied Physics, School of Physical and Mathematical Sciences, Nanyang Technological University, Singapore 637371*

**Email : csoci@ntu.edu.sg*

Section 1. Structural and optical characterization of the polycrystalline $MAPbI_3$ film

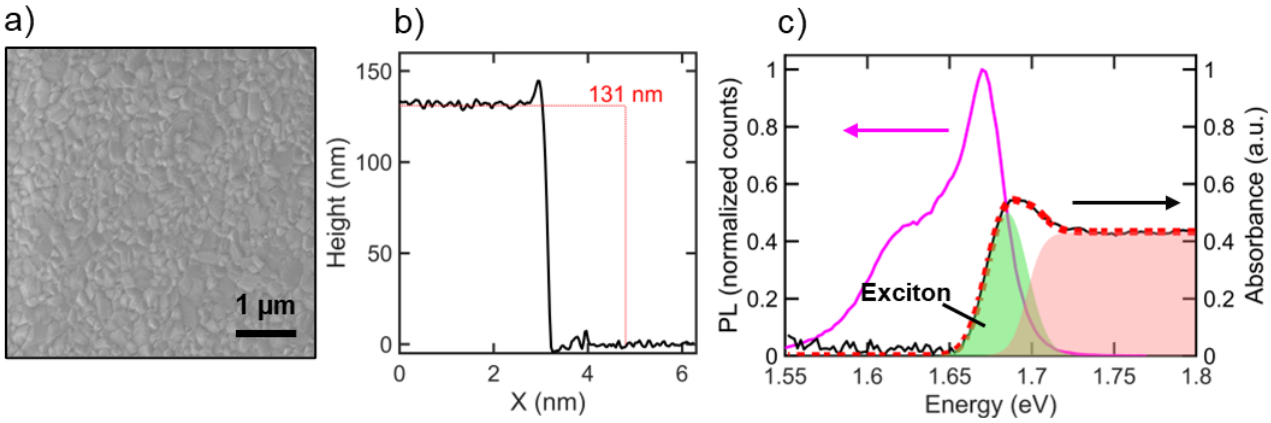

Figure S1: **(a)** Scanning electron microscope image of the polycrystalline perovskite film showing sub-micron grain size. **(b)** Thickness profile of the perovskite film obtained by atomic force microscopy area scan. The film thickness is of 131 nm, and the absolute roughness about 5 nm. **(c)** Photoluminescence (blue) and absorbance (black) spectra of the $MAPbI_3$ perovskite film at 77 K. The red dashed line is the fit of the absorbance spectrum that includes the contributions from the exciton (green shaded area) and the continuum (grey shaded area) states, using the Elliott's model.

Section 2. Metasurface design

The qBIC metasurface consists of a square lattice with period $\mathrm{p} = 380\ \mathrm{nm}$ of isosceles triangular holes of height and base length $\mathrm{a} = 200\ \mathrm{nm}$. The qBIC resonance arises from a near-field out-of-plane magnetic quadrupole (**Fig. S2a**), that exhibits a slightly asymmetric distribution in the $x-y$ plane, due to the broken in-plane inversion symmetry of the design. Through eigenfrequency simulation, it is possible to compute the total complex electric field $\tilde{E}(x,y) = E_x(x,y) + i\tilde{E}_y(x,y)$ across all frequencies and points in momentum space. The field distributions in the circular polarization basis are computed through Jones calculus:

$$|LC\rangle = \frac{1}{2}\begin{pmatrix}1 & 0\\ 0 & 0\end{pmatrix}\begin{pmatrix}1 & -i\\ i & 1\end{pmatrix}\tilde{E}(x,y)$$

$$|RC\rangle = \frac{1}{2}\begin{pmatrix}1 & 0\\ 0 & 0\end{pmatrix}\begin{pmatrix}1 & i\\ -i & 1\end{pmatrix}\tilde{E}(x,y)$$

The calculated intensities of $|\mathrm{LC}\rangle$ and $|\mathrm{RC}\rangle$ are illustrated in **Fig. S2b,c** respectively. **Fig. S2d** illustrates the polarization ellipses distribution in momentum space, highlighting two singularities at $k_x = \pm\, 0.38\ \mu m^{-1}$ (positive for $|LC\rangle$ and negative for $|RC\rangle$). **Fig. S2e** depicts the numerically simulated distribution of the Q-factor across k-space, which reaches a maximum at Γ but remains sufficiently high off- Γ, effectively confining light in regions of high spin purity.

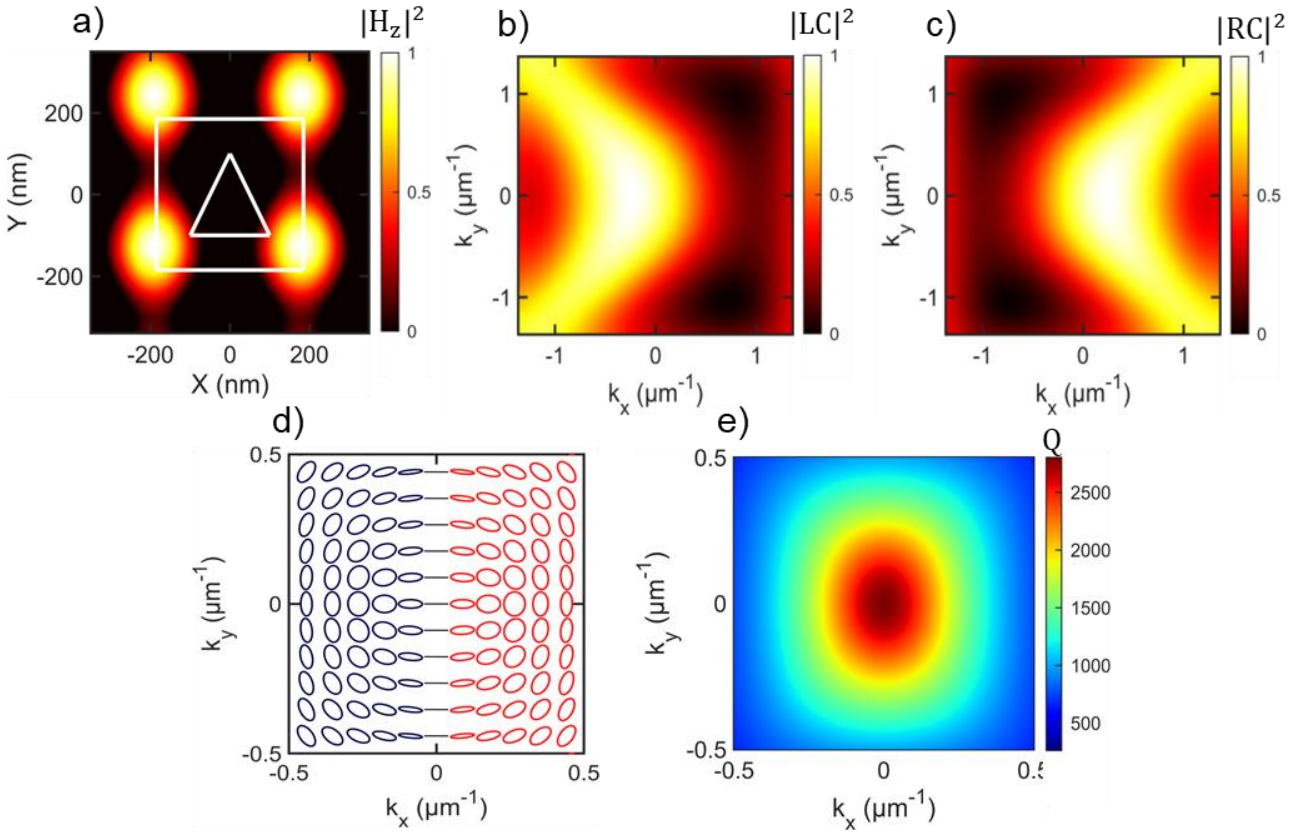

Figure S2: **(a)** Simulated in-plane distribution of the near-field out-of-plane magnetic field H_z of the *q*BIC resonance. **(b-c)** Intensity distributions of the field in the circular polarization basis, retrieved from the simulated total complex electric field. **(d)** Momentum space distribution of the polarization ellipses, highlighting the presence of two off-Γ circularly polarized states. **(e)** Momentum space distribution of the Q-factor of the *q*BIC resonance.

Section 3. Coupled oscillator model and polariton bands fitting

The strong coupling regime in the *q*BIC metasurface is evidenced by fitting the band dispersions with a coupled oscillator model describing the interaction between the $MAPbI_3$ exciton and the *q*BIC photonic mode, following the approach adopted in our previous work (Ref. 42 in the main text). From the Elliots' model fit in **Fig. S1c**, we extract the $MAPbI_3$ exciton resonance position $E_{exc} = 1.685$ eV and its linewidth $\gamma_{exc} = 0.028$ eV. The dispersion of the uncoupled photonic mode is linearly extrapolated from the lower polariton band at momenta ($k_x \gg 0$) where the exciton contribution is negligible and the band is purely photonic. The mode is characterized by an average linewidth $\gamma_c = 0.0094$ eV. The exciton-*q*BIC interaction is modelled by the coupled oscillator, which predicts the formation of the upper and lower exciton-polariton bands:

$$E_{LP,UP} = \frac{1}{2}\left[E_{exc} + E_{cav} + \frac{i(\gamma_{cav} + \gamma_{exc})}{2}\right] \pm \sqrt{g^2 + \frac{1}{4}[E_{exc} - E_{cav} + i(\gamma_{cav} - \gamma_{exc})]^2}$$

By substituting the experimentally determined energies and linewidths into the model, the coupling strength, *g* remains the sole fitting parameter. This is thus determined by minimizing the error between the calculated lower polariton dispersion and the experimental lower polariton emission. The Rabi splitting, $\hbar\Omega$, is then obtained from:

$$\hbar\Omega = 2\sqrt{g^2 + \frac{(\gamma_{cav} - \gamma_{exc})^2}{4}}.$$

The upper polariton is not observed due to the strong absorption of the $MAPbI_3$ film in the predicted spectral region. Our coupled oscillator model is further validated by independent simulations of the polariton bands using two complementary approaches, RCWA (**Fig. S3a**) and COMSOL eigenfrequency analysis (**Fig. S3b**). By adopting the refractive index of $MAPbI_3$ reported in the literature at 77 K[1], we obtain polariton dispersions that perfectly overlap with the bands extracted from fitting the experimental data, confirming the accuracy of our model.

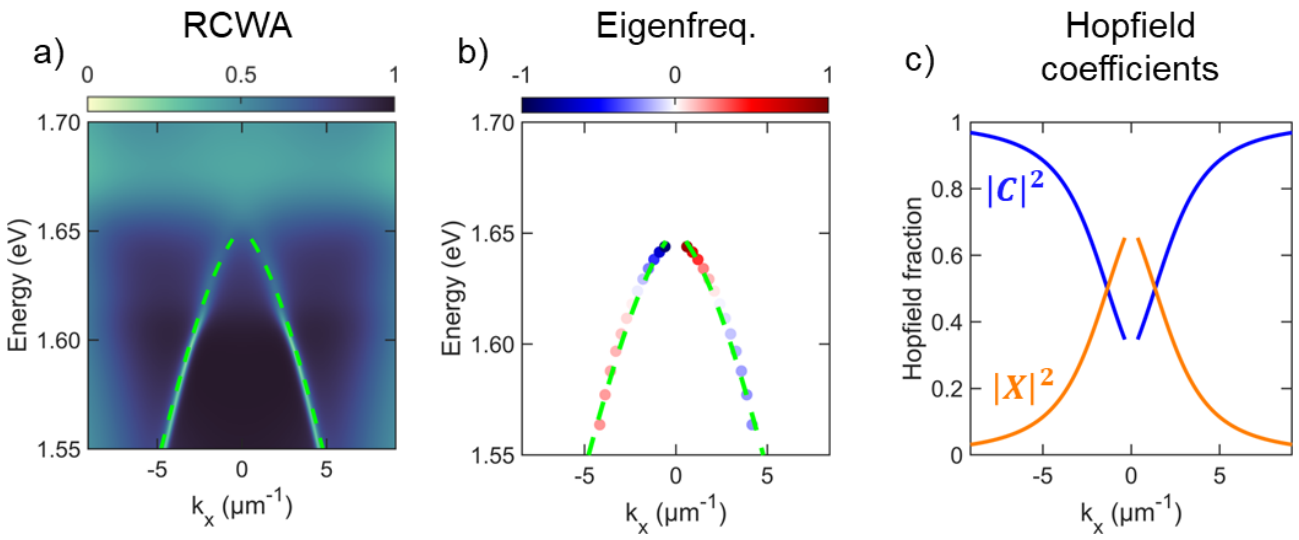

Figure S3: (a) RCWA simulation of the angle-resolved transmittance spectrum and **(b)** eigenfrequency simulation of the band in the momentum space showing perfect overlap with the polariton band extracted from the coupled oscillator model. **(c)** Calculated Hopfield coefficients of the *q*BIC polariton band.

Fig. S3c illustrates the Hopfield coefficient of the *q*BIC lower polariton branch, calculated as:

$$|C|^2 = \frac{1}{2}\left(1 - \frac{\Delta(k_x)}{\sqrt{\Delta(k_x)^2 + (2\hbar\Omega)^2}}\right)$$

$$|X|^2 = \frac{1}{2}\left(1 + \frac{\Delta(k_x)}{\sqrt{\Delta(k_x)^2 + (2\hbar\Omega)^2}}\right)$$

with $\Delta(k_x)$ is the difference of the cavity dispersion and the exciton resonance. The lower polariton band exhibits large excitonic fraction in the vicinity of the Brillouin zone centre. This feature provides an efficient relaxation pathways to the ground state, a condition which favours exciton-polariton condensation with low excitation fluence thresholds.[2]

Section 4. Experimental setups

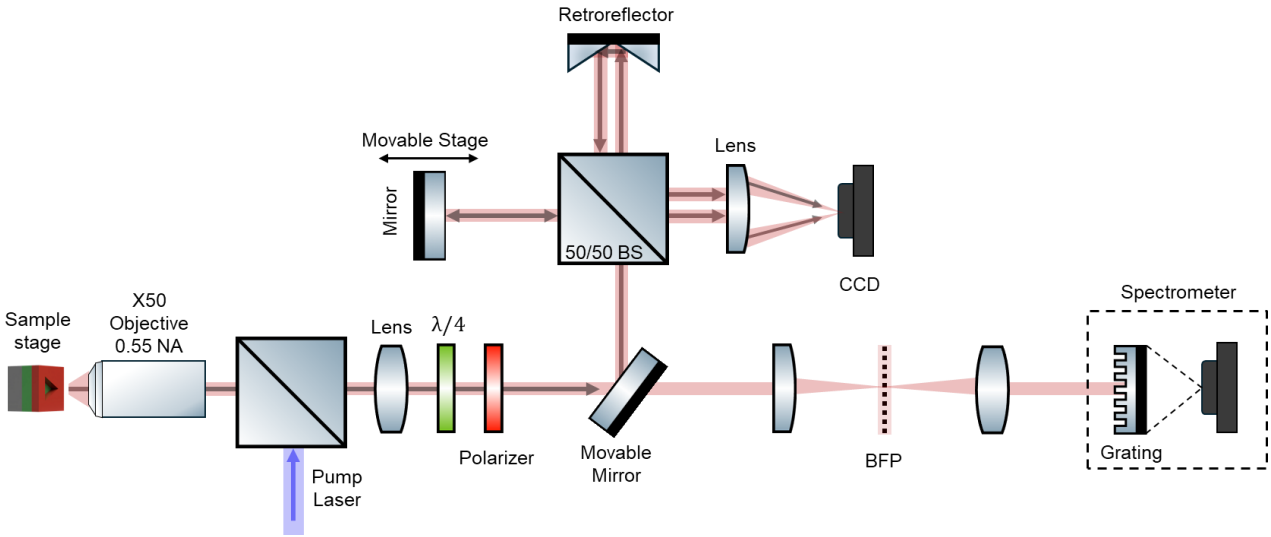

Figure S4: Schematic of the Fourier imaging setup used to measure the angle-resolved reflectance and photoluminescence bands of the metasurfaces. A Michelson interferometer is inserted into the collection path via a movable mirror to measure the temporal and spatial coherence of the polariton condensate.

Section 5. Polariton condensate analysis

The integrated photoluminescence emission as a function of excitation fluence shown in **Fig. S5a**, present the characteristic sigmoidal shape of the polariton lasing. After an initial linear growth, the intensity shows a superlinear trend after the excitation threshold $P_{th} = 26.9\ \mu J/cm^{-2}$, accompanied by a sudden linewidth reduction (**Fig. S5b**). Hallmark signature of polariton condensation is the peak emission blueshift (**Fig. S5c**), due to the non-linear stimulated scattering processing that determines the onset of the condensate phase transition.

The temporal and spatial coherences of the polariton condensate are measured through Michelson interferometry, where a beam splitter separates the emitted signal into two arms with tunable distance. Before being recombined on a CCD camera, the wavefront of the beam in one of the two arms is flipped along one axis, using a retroreflector. By tuning the path difference, Δx, between the two arms of the interferometer, it is possible to observe the formation of distinct interference fringes at the position of maximum overlap between the two beams $\Delta x = 0\ \mu m$ (**Fig. S5d**). A spatial coherence of $9.85\ \mu m$ was estimated by Gaussian fitting of the Fourier transform of the interference fringes at $\Delta x = 0\ \mu m$ (**Fig. S5e**). A temporal coherence of $509\ fs$ is evaluated by measuring the visibility of the fringes as function of the temporal delay between the two arms of the interferometer.

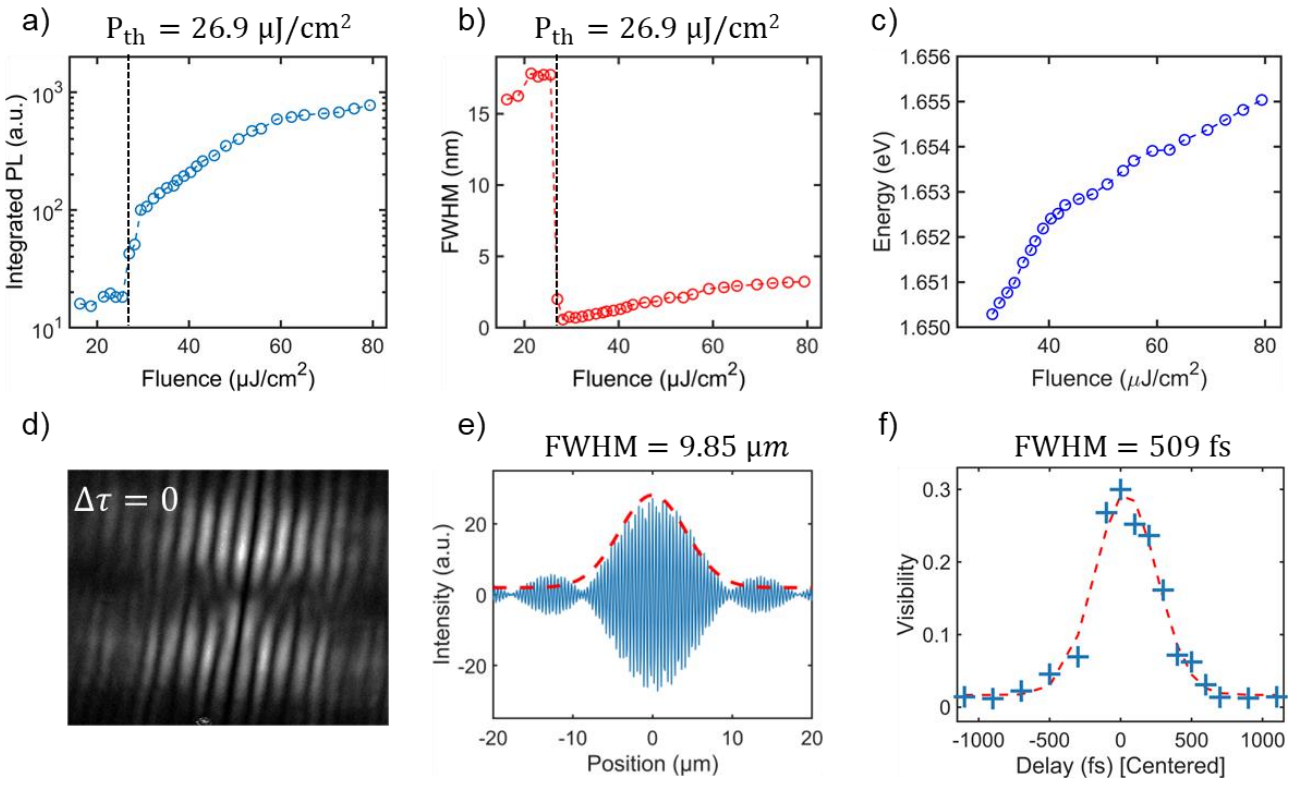

Figure S5: **(a)** Integrated photoluminescence intensity, **(b)** linewidth, and **(c)** blueshift of the energy peak as function of excitation fluence. **(d)** Real space image, recorded on a CCD array, of the spatially superimposed emission of two arms in the Michelson interferometer at $\Delta x = 0$ μm, with the typical interference fringes pattern. **(e)** Spatial and **(f)** temporal coherence of polariton emission.

Section 6. Stokes polarimetry

The characterization of the k-space polarization pattern is carried out with standard Stokes polarimetry. The Stokes parameters are retrieved through intensity measurements in 6 polarization bases: horizontal (H), vertical (V), diagonal (D), anti-diagonal (A), left- (L) and right-handed (R) circular polarization:

$$S_1 = \frac{H-V}{H+V}, \qquad S_2 = \frac{D-A}{D+A}, \qquad S_3 = \frac{L-R}{L+R}$$

Where the degree of circular polarization is S_3 ranging from -1 (RCP) to +1 (LCP), and the Stokes phase is given by $\varphi_s = \mathrm{atan}(S_2, S)$, which is singular at the points of pure circular polarization.

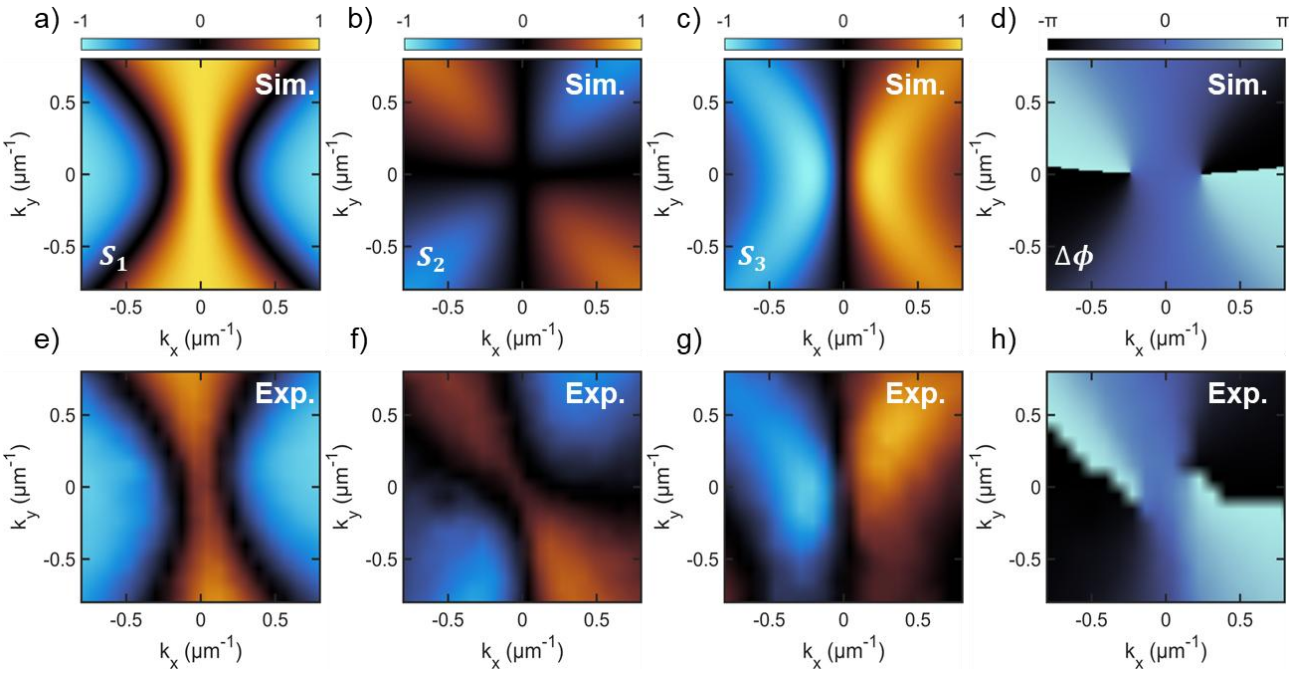

Figure S6: **(a–c)** Simulated angle-resolved Stokes parameters S_1, S_2, S_3 in the reciprocal space. **(e)** Calculated phase φ_s. (**e–g**) Experimental Stokes polarimetry and **(h)** phase retrieval revealing a complex polarization distribution of the condensate emission and the presence of phase spin vortices.

Section 7. Simulation of real space phase vortices

The ideal profile at k-space is obtained from the simulation of the metasurface polarization eigenmodes illuminated by a plane wave at different incidence angles. The maximum simulated wavenumber was $\mathrm{k_{max}} = 0.08 \cdot \frac{2\pi}{\mathrm{p}}$ with p the length of the unit cell. The simulated wavefunction at *k*-space has both left and right circularly polarized scalar components. To replicate the experimental results obtained from the Michelson interferometry, we first project the wavefunction into one of the circular polarized components (signal) and we let it interfere it with its mirror image (reference), mimicking the effect of the retroreflector. The reference is set with a small propagation direction mismatch, carrying an extra linear phase factor $\exp\big(i(\kappa_x X + \kappa_y Y)\big)$ which leads to the interference fringes, as in experimental conditions. The factors κ_x and κ_y are proportional to the spatial shift introduced by the retroreflector in the X and Y directions, which become a phase shift at the focal plane of the lens. For sake of simplicity, we set these two factors manually in the simulation. The ideal self-interference intensity patterns are shown in **Fig. S7a-c** for LCP, linear and RCP polarization basis, respectively. The spin-orbit coupling is evidently shown in the k-space profiles as opposite circular polarizations travel with opposite momentum, appearing at opposite sides of the k-space, each of them carrying an optical vortex with conjugate topological charge (**Fig. S7d-f**), and no vortices are observed for linear polarization (**Fig. S7e**). The real space profiles are obtained by inverse Fourier transform of the k-space pattern, simulated as a $2f$-focusing system with standard Fourier optics diffraction integrals: the fields are first propagated in free-space a distance f, then they are multiplied by the lens transfer function $\exp\left(-\frac{ik(x^2+y^2)}{2f}\right)$ followed by the propagation of another free-space distance f. The value of the focal length f is arbitrary and only scales transversally the profiles. To avoid aliasing artifacts, the *k*-space profiles are modulated by a Gaussian apodization profile $A(r) = \exp(-r^2/w_0^2)$ of width $w_0 \approx k_{\max}$ so that practically all the area of the simulated *k*-space is captured. As the value of the focal length *f* only scales the size of the pattern, for simplicity the focal length *f* is chosen to match the Rayleigh range of the apodization function $f = \pi w_0^2/\lambda$, so

that real space and *k*-space images have similar size, simplifying the mesh requirements. To replicate experimental conditions, each polarization component is again interfered with its mirror image having a small propagation direction mismatch at the detection plane, leading to interference fringes. To account for the possible angle mismatch before the last lens focuses the profiles (which leads to spatial shifts at the detector plane), we also introduce a spatial shift in real space, which is responsible for the splitting of the second order phase singularities into two phase singularities of first order. This high order singularity splitting is in any case a natural phenomenon which will be unavoidably present in experiments. The simulation results of real-space self-interference are shown in **Fig S8a-c** shows the interference fringes for left-circular, linear and right-circular polarizations, and their corresponding phase profiles are shown in **Fig. S8d-f**. All phase profiles are obtained by off-axis phase retrieval with Fourier transform as explained in the main text.

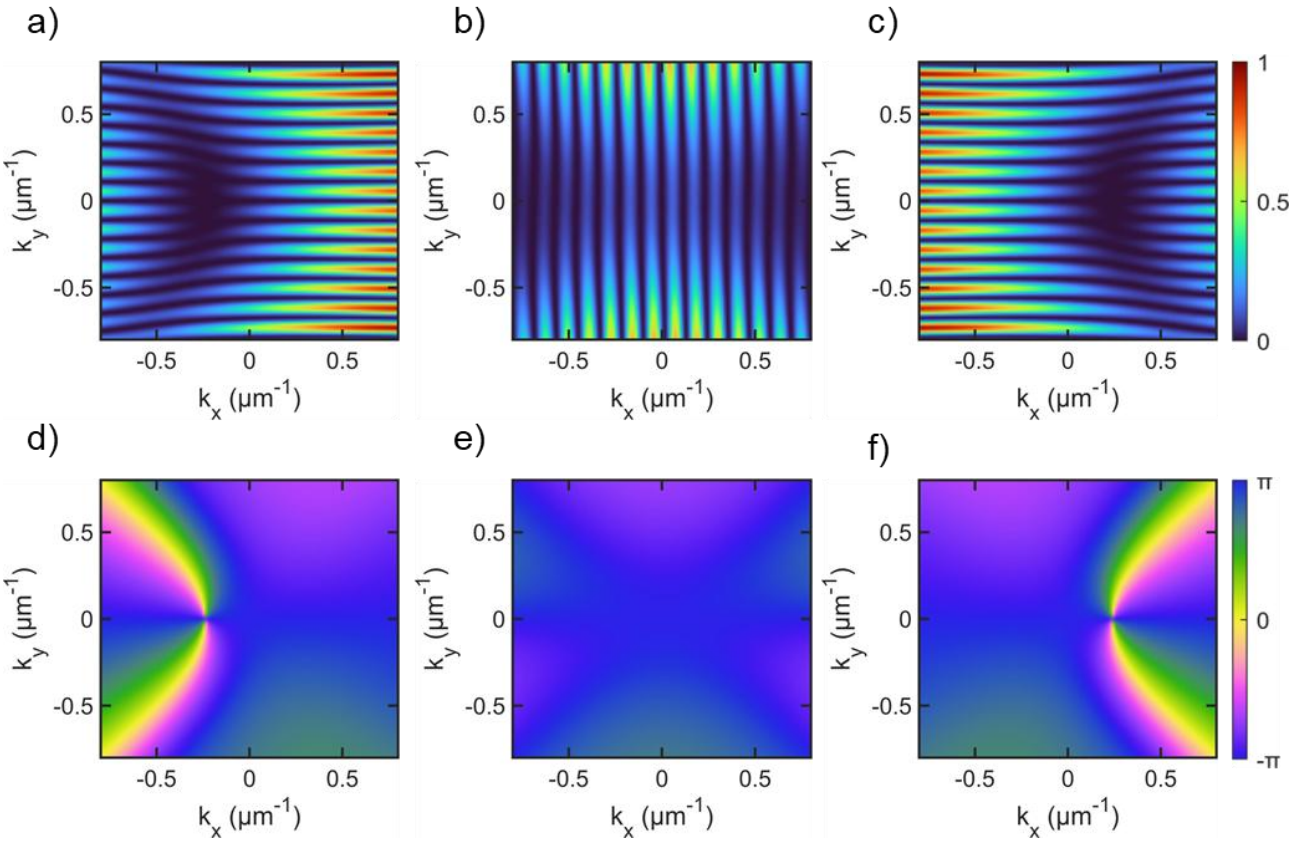

Figure S7: **(a-c)** Simulated interference fringes in the momentum space for LCP **(a)**, RCP **(c)** and the overlap of the two **(b)**. **(d-f)** Calculated phase distribution with an appearance of topological charges for LCP **(d)**, RCP **(f)** and the overlap of the two **(e)**.

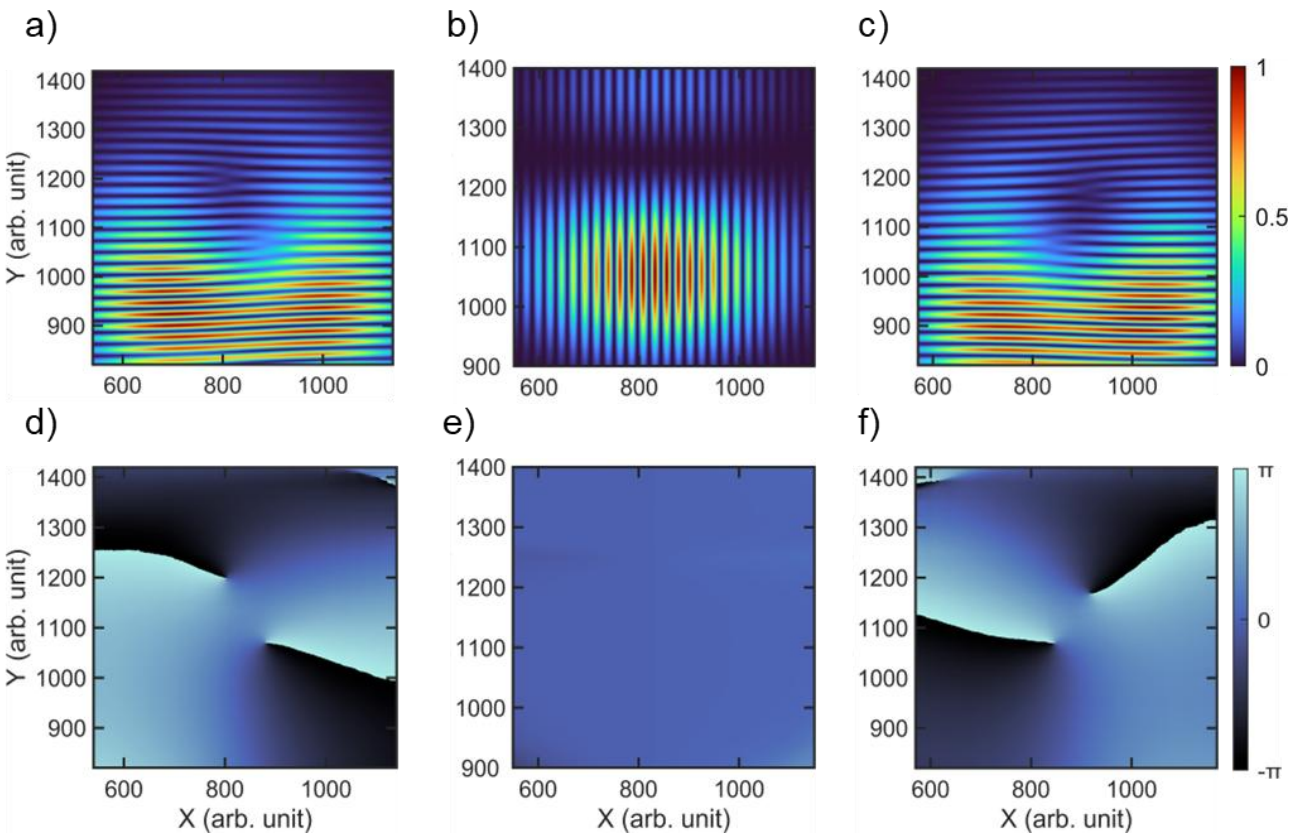

Figure S8: **(a-c)** Simulated interference fringes in the real space for LCP **(a)**, RCP **(c)** and the overlap of the two **(b)**. **(d-f)** Calculated phase distribution with an appearance of topological charges for LCP **(d)**, RCP **(f)** and the overlap of the two **(e)**.

Section 8. Vortices characterization and healing length calculation

Within the hydrodynamics description of a quantum fluid, the condensate velocity field is proportional to the gradient of the phase of the field $\nabla\phi$. In cylindrical coordinates, the gradient is dependent to the inverse of the radius r. As a result, in presence of a vortex the velocity, and hence the local kinetic energy, formally diverge as $r \to 0$, that is, at the centre of the vortex core. This divergence is avoided by the vanishing of the condensate density density $|\Psi|^2$ at the core centre[3,4]. The dips in the density are shown in **Fig. S9.a** corresponding to the same locations identified for the σ^+ vortex in **Fig. 3b,c** and for σ^- vortex in **Fig. 3e,f**. **Fig. S9b,c** illustrate the density line profiles along the x- and y-directions for the σ^+ and σ^- vortices, respectively, from which a FWHM of 1.7 μm is extracted, corresponding to the radius of the vortex cores. The core radius is used to compare the healing length shown in **Fig. 4f**. As definition,

$$\xi = \frac{\hbar}{\sqrt{2 \cdot {m_{LP}}^* \cdot g \cdot n}}$$

where ${m_{LP}}^*$ is the effective mass of the lower polariton branch, g is the coupling strength, and n is the polariton density. Under resonant excitation, the interaction energy satisfies $g_r \cdot n = \Delta E$ with ΔE the observed emission peak blueshift, that directly reflects polariton- polariton interactions within the condensate. Under non-resonant excitation, the coupling strength constant g_{nr} also accounts the polariton-reservoir interactions, which formally invalidating the previous linear dependence. However, within the excitation fluence range investigated, from 32 to 42 μJ/cm^2, the blueshift exhibits an approximately linear dependence on fluence, thereby justifying the use of the relation $g_{nr} \cdot n \cong \Delta E$ as a good approximation. The effective mass of the lower polariton branch is obtained from the curvature of its experimental dispersion at the condensation wavevector, according to

$$\frac{1}{{m_{LP}}^*} = \frac{1}{\hbar^2}\left[\frac{\partial^2 E_{LP}}{\partial k^2}\right]_{k=Cond.}$$

and it is equal to $|{m_{LP}}^*| = 1.526 \times 10^{-5}\ m_e$, comparable for other perovskite polariton condensates.

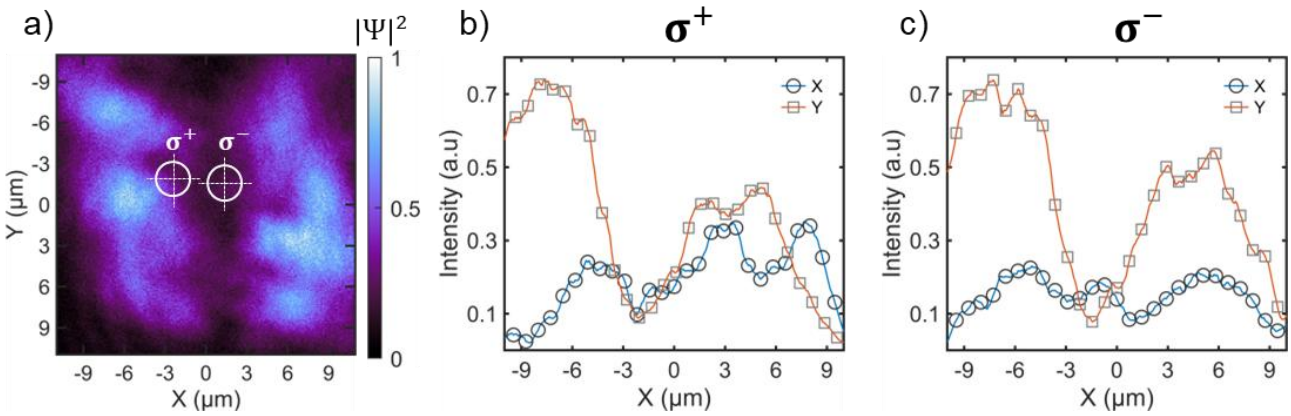

Figure S9: **(a)** Real space image of the condensate emission where the dips in intensities are identified on the lobes with opposite spin. **(b-c)** Line profiles in the x- and y-directions for the σ^+ and σ^- vortices, respectively.

References

1. Jiang, Y. *et al.* Temperature dependent optical properties of CH3NH3PbI3 perovskite by spectroscopic ellipsometry. *Appl. Phys. Lett.* **108**, 061905 (2016).
2. Deng, H., Haug, H. & Yamamoto, Y. Exciton-polariton Bose-Einstein condensation. *Rev. Mod. Phys.* **82**, 1489–1537 (2010).
3. Timofeev, V. & Sanvitto, D. *Exciton Polaritons in Microcavities: New Frontiers*. (Springer Berlin Heidelberg, Berlin, Heidelberg, 2012). doi:10.1007/978-3-642-24186-4.
4. Lagoudakis, K. G. *et al.* Quantized vortices in an exciton–polariton condensate. *Nat. Phys.* **4**, 706–710 (2008).